

JaGuard: Jamming Correction of GNSS Deviation with Deep Temporal Graphs

Ivana Kesić*, Aljaž Blatnik†, Carolina Fortuna* and Blaž Bertalanšč*

*Department of Communication Systems, Jožef Stefan Institute, Slovenia

†Faculty of Electrical Engineering, University of Ljubljana, Slovenia

{blaz.bertalanic, carolina.fortuna}@tjjs.si

Abstract—Global Navigation Satellite Systems (GNSS) face growing disruption from intentional jamming, undermining availability exactly when reliable positioning and timing are essential. We tackle this challenge by recasting jamming mitigation as a dynamic graph regression problem and propose a Jamming Guardian (JaGuard), a new receiver-centric deep temporal graph network-based method that estimates, and thereby corrects, the receiver’s latitude and longitude errors. At each 1 Hz epoch, we model the satellite–receiver scene as a heterogeneous star graph with the receiver as the center node and the tracked satellites as leaves. These satellites have time-varying attributes such as SNR, azimuth, elevation, and latitude/longitude. A single-layer Heterogeneous Graph ConvLSTM (HeteroGCLSTM) fuses one-hop spatial context with short-term temporal dynamics to produce a 2D deviation vector for error mitigation. We evaluate our approach on datasets collected from physical hardware (two different commercial receivers), subjected to controlled conducted RF interference. Interference is introduced with three jammer types: Continuous Wave CW, multi-tone $3\times$ CW, and wideband FM. Each jammer type was exercised at six power levels from -45 to -70 dBm, with 50 repetitions per scenario, including pre-jam, jam, and recovery phases. Compared to strong multivariate time series baselines (TSMixer MLP, uniform CNN, and Seq2Point CNN), our model consistently yields the lowest Mean Absolute Error (MAE) in positional deviation. Under severe jamming at -45 dBm, it achieves an MAE of 3.64–7.74 cm across all device and jammer combinations, improving to 1.59–1.90 cm at lower power levels of -60 to -70 dBm. On mixed-mode datasets that pool all power levels, the MAE is 3.78 cm for GP01 and 4.25 cm for U-blox 10, surpassing Seq2Point, TSMixer, and uniform CNN. A data-efficiency split further shows that with only 10% of the training data, our approach remains clearly ahead, achieving an MAE of about 20 cm versus 36–42 cm for the baselines.

Index Terms—time series, gnss, jamming, graph neural networks, dynamic temporal graphs

I. INTRODUCTION

Global Navigation Satellite Systems (GNSS) underpin nearly every critical infrastructure, from telecommunications [1] and aviation safety [2], power-grid synchronization [3], emerging drone ecosystems where location privacy and integrity are paramount [4], to autonomous driving [5]. As GNSS becomes more deeply integrated into real-time control systems, its evolution from convenient enabler to potential systemic reliability threat is becoming increasingly visible. Correspondingly, GNSS interference incidents have surged, with recent reports documenting a *five-fold increase* in large-scale interference affecting civil aviation and regional systems in 2024 [2]. The scale and frequency of these events indicate that

GNSS disruptions are no longer isolated anomalies but a persistent operational hazard. In aerospace and other navigation-critical domains, even short periods of GNSS degradation can force transitions to reversionary modes, compromise guidance integrity, or increase required separation, making interference resilience a central systems-engineering challenge.

The fundamental vulnerability arises from the extremely weak power levels at which GNSS signals are received. This inherent weakness is further exacerbated by satellite aging, which leads to power source degradation and progressively weaker signal transmission capabilities [6]. Consequently, even modest interference can degrade correlation, suppress the effective Signal-to-Noise ratio (SNR), and destabilize code or carrier tracking loops. Among interference mechanisms, jamming remains the most disruptive in practice [7], as recent advances in low-cost software-defined radios (SDRs) enable agile, programmable jammers capable of sweeping, modulating, or hopping frequencies that are inexpensive and easy to deploy [8]. Although receivers incorporate basic anti-jamming measures through spread-spectrum modulation and correlation techniques [9], these mechanisms were designed for earlier interference environments. Contemporary threats increasingly exceed the capabilities of traditional filtering, blanking, or threshold-based detectors [10]. Data-driven mitigation approaches have therefore emerged, broadly targeting three objectives: anomaly detection [11], [12], position forecasting [13], and position error correction [14]. While anomaly detection offers situational awareness, it often triggers exclusion or denial-of-service responses. Forecasting absolute coordinates is unstable under non-stationary interference because historical errors propagate forward. Recent work on position-error correction provides more stable behavior but remains largely static, relying on per-time step observations.

We noticed that modeling the temporal evolution of interference, that causes GNSS degradation, is yet to be considered as dynamic. A key yet underutilized property of GNSS measurements is their spatiotemporal coherence. Because the GNSS constellation moves continuously relative to the receiver, measurement quality exhibits coherent temporal structure under nominal conditions. Jamming disrupts this structure, as satellites can appear to rise and set erratically within short intervals, causing abrupt changes in both visibility and signal attributes. This produces a time-varying star topology in which satellite nodes show correlated, interference-driven fluctuations. Interpreting this constellation–receiver interaction

as a dynamic graph offers a principled means of capturing these spatiotemporal distortions and their effect on position error.

Motivated by these considerations, we formulate GNSS jamming mitigation as a dynamic temporal graph regression problem. Our receiver-centric model exploits short histories of constellation evolution to estimate the horizontal position deviation. Such targeted error estimation supports resilient navigation in aerospace, automotive, maritime, and other safety-critical systems where GNSS degradation must be mitigated rather than merely detected. The main contributions of this paper are:

- This paper is the first to frame the GNSS jamming position error correction as a dynamic temporal graph regression problem, representing the evolving satellite–receiver interaction space as a sequence of heterogeneous graphs that capture both spatial and temporal dependencies.
- We propose Jamming Guardian (JaGuard), a Heterogeneous Graph Convolutional Long Short-Term Memory (HeteroGCLSTM) method that jointly learns from the constellation’s spatial topology and short-term temporal dynamics, enabling direct estimation of latitude and longitude deviation error.
- We conduct a large-scale experimental evaluation using a real-world dual-receiver, multi-jammer dataset collected under controlled jamming interference. The dataset covers three jamming types, six jamming power levels (-45 to -70 dBm), and 50 repetitions per configuration, enabling rigorous analysis.
- Under heavy jamming, the model achieves 3–7 cm mean absolute error (MAE), consistently outperforming advanced time-series baselines. Even with only 10% of the training data, it retains a clear performance margin, showing excellent data efficiency.
- The proposed model maintains sub-10 cm accuracy when transferred between receivers and under unseen interference types, demonstrating strong generalization across hardware and environmental conditions.

This paper is organized as follows. The related work is discussed in Section II. Section III provides the problem formulation, while Section IV elaborates on the proposed time series to temporal graph transformation. Section IV-A introduces the architecture of the proposed model, Section V describes the relevant methodological and experimental details, while Section VI provides a thorough analysis of the results. Section VII details the operational boundaries of the proposed method. Finally, Section VIII concludes the paper.

II. RELATED WORK

Accurate GNSS position and timing information are essential for scientific and safety-critical applications thus ensuring the reliability of this information against interference is a primary research objective. Current research efforts within this field largely concentrate on three principal goals: (1) detecting anomalies, (2) forecasting absolute position, and (3) a more recent focus on the direct correction of positional error. Table I summarizes the most relevant works. The first column lists the

authors, the second specifies the problem type they solved. The third column presents the approach they used, broken down by the type of input data and the utilized method.

As shown in the second column of Table I, a major portion of the literature is dedicated to the problem of *anomaly detection*, which focuses on identifying anomalies within the receiver’s processed data. The detection of anomalies typically serves three primary purposes: retrospective data correction [11] [12], real-time data pruning [15], or event classification and flagging for subsequent analysis [16] [17].

The goal of data correction is to improve the overall quality of a dataset in post-processing. This was exemplified by the work of Li et al. [11], who applied a Hampel filter to a GNSS coordinate time series to detect and eliminate anomalous outliers, followed by KNN smoothing to further reduce residual noise, reporting cleaner, more stable coordinate traces. Similarly, Liu et al. [12] also exemplify retrospective data correction on smartphone GNSS data in urban environments. They first identify Non-Line-of-Sight (NLOS) signals and then correct the underlying pseudorange measurements, the satellite-to-receiver distance estimates, using a Convolutional Neural Network (CNN) for detection and Variational Mode Decomposition (VMD) for data correction. NLOS signals are, in their core, anomalies caused by reflections from urban structures that elongate the signal path.

Xia et al. [15] demonstrate the use of anomaly detection for the purpose of real-time data pruning. Their key contribution is a system that uses unsupervised clustering (HDBSCAN) to automatically label vehicle-mounted GNSS data in urban environments affected by NLOS. On those labels, a supervised classifier is then trained to identify and remove anomalous NLOS observations from the live positioning calculations.

The third application of anomaly detection is to classify or flag events for later analysis. For instance, the pipeline by Mehr et al. [16] classifies the specific type of interference directly from the raw signal, providing crucial information for threat assessment. This classification approach is also central to the work of Ivanov et al. [17], who offer a methodological critique against the trend of using overly complex deep learning models, such as the multi-stage pipelines previously mentioned for this task. Ivanov et al. [17] demonstrate that a simple classifier trained on statistical features summarizing an entire flight can achieve superior performance in flagging anomalous recordings for post-flight review. While effective, all approaches within this problem space are fundamentally reactive or exclusionary.

Position forecasting constitutes the second problem type addressed in the literature. The goal of these methods is to predict the receiver’s absolute coordinates from historical measurements. A common strategy is a “decompose then predict” approach, used by both Zhou et al. [13] and Chen et al. [18] to forecast the absolute coordinates of stationary GNSS stations. They first use signal decomposition techniques (EEMD and VMD, respectively) to break the time series into simpler components, and then train separate LSTM networks to forecast each E/N/U (East, North, Up) coordinate component individually. Another strategy involves manual feature engineering, as demonstrated by Gao et al. [19] in their

Work	Goal	Method Category	Model	Input
Li <i>et al.</i> [11]	AD	Statistical/ML	Hampel Filter + KNN	UTS
Liu <i>et al.</i> [12]	AD	Signal Processing + DL	VMD + CNN	MTS
Xia <i>et al.</i> [15]	AD	Unsupervised + Supervised ML	HDBSCAN + Classifier	MTS
Mehr <i>et al.</i> [16]	AD	Deep Learning	LSTM-Autoencoder + CNN	MTS
Ivanov <i>et al.</i> [17]	AD	Supervised ML	LightGBM	Statistical Features
Zhou <i>et al.</i> [13]	PF	Signal Processing + DL	EEMD + LSTM	UTS
Chen <i>et al.</i> [18]	PF	Signal Processing + DL	VMD + LSTM	UTS
Gao <i>et al.</i> [19]	PF	Supervised ML	GBDT, LSTM, SVM	MTS + External Features
Kanhere <i>et al.</i> [14]	PEC	Deep Learning	Set-based DNN	Pseudorange Residuals, LOS
Zhu <i>et al.</i> [20]	PEC	Deep Learning	Transformer	MTS
Mohanty <i>et al.</i> [21]	PEC	Deep Learning	GCNN	Graph (Satellite Features)
This work	PEC	Deep Learning	Temporal Graph NN	DHG

TABLE I: Summary of the related work in data-driven GNSS mitigation.

* AD (Anomaly Detection), PF (Position Forecasting), PEC (Position Error Correction), UTS (Univariate Time Series), MTS (Multivariate Time Series), DHG (Dynamic Heterogeneous Graph), SP (Signal Processing), ML (Machine Learning), DL (Deep Learning), LOS (Line-of-Sight).

prediction of vertical displacement. Their main innovation is to augment the time series with a diverse set of external physical variables known to influence crustal movement, such as atmospheric pressure and temperature. However, these forecasting-based methods have several drawbacks. First, they rely on extensive pre-processing or feature engineering that may not generalize. More importantly, forecasting absolute position is an inherently unstable task [22]. The underlying signal is non-stationary, and any subtle, uncorrected errors in the historical data, which detection methods might miss, are compounded by the forecasting model, leading to rapid predictive drift rather than reliable correction.

This motivates a third problem category named *position error correction*. Instead of forecasting a high-drift, absolute position, this approach predicts the error deviation of longitude and latitude. This reframes the task as a more stable regression problem, where the model learns to anticipate the effect of interference and provides a direct correction. For example, Kanhere et al. [14] designed a set-based Deep Neural Network (DNN) to estimate 3D position corrections from pseudorange residuals and satellite line-of-sight vectors. Zhu et al. [20] employ a Transformer-based network (T-GPCN) for the same purpose, reformulating the regression as a classification task to improve convergence. In addition, this problem has also been a target for Graph Neural Networks (GNN)s, as [21] demonstrated a GNN approach to learn position corrections from noisy smartphone GNSS data, using a graph to represent spatial relationships between satellites. Although these architectures offer promising directions for multipath mitigation, their underlying design assumptions make them unsuitable for jamming-focused scenarios. Architectures such as [14] and [21] strictly require raw measurements, specifically pseudorange residuals, Doppler and Carrier Phase (ADR) data, which are inputs unavailable in our standard NMEA-level observation setting. Furthermore, they assume a reliable initial position for linearization or Kalman filtering, an assumption that collapses under strong jamming regimes. Beyond these input constraints, the satellite-mesh topology in [21] presents a structural incompatibility. While valid for geometric correlations such as multipath, it fails to capture the receiver-centric

nature of jamming, which degrades the downlink rather than the inter-satellite links.

Gap identification: Taken together, these limitations reveal a broader blind spot in current GNSS mitigation research: existing methods, whether based on anomaly detection, forecasting, or position-error correction, largely ignore the spatiotemporal structure of jamming. Anomaly-detection pipelines operate purely reactively, identifying or excluding corrupted samples without reconstructing the underlying trajectory. Forecasting approaches attempt to predict absolute coordinates from historical measurements, but the non-stationary nature of GNSS signals causes these models to amplify rather than correct errors once jamming distorts the history. Even the most advanced GNN-based PEC methods [21] remain temporally static, as they process each epoch independently. This time-agnostic perspective fails to capture the rapid disruption of spatiotemporal coherence and the erratic constellation changes caused by jamming. Consequently, to the best of our knowledge, no prior work has formulated GNSS jamming mitigation as a dynamic temporal graph regression problem. While spatiotemporal GNN have been explored in other domains, their application to GNSS jamming remains unaddressed. This paper fills that gap by proposing a temporal GNN architecture that leverages the receiver-centric star topology to jointly model the constellation’s evolving geometry and its short-term history, enabling the system to capture the time-correlated, structure-breaking distortions that previous approaches overlook.

III. PROBLEM FORMULATION

GNSS signals arrive at very low power due to orbital free-space loss and spread-spectrum transmission, which is why the received L1 signal is typically below the receiver’s intrinsic noise floor. Receivers recover them by correlating the incoming signal with each satellite’s spreading code and integrating over short intervals, allowing the correlation peak to rise above the noise. Any additional radio energy in the L1 band, the main civil GNSS band at ~ 1575.42 MHz, is referred to as jamming and acts as added noise: it lowers the effective SNR and makes it difficult to keep a reliable lock on each satellite.

Figure 1 illustrates a spectral view of the L1 GNSS band, showing how different types of jamming profiles overlay the GNSS signal spectrum [23]. The dashed black line indicates the standard GNSS spectrum, while the colored traces represent different jamming profiles. Shown in red trace is a Continuous Wave signal (CW), a very narrow-band, single-tone jammer that appears as a sharp spectral spike. The blue trace is a multi-tone $3\times\text{CW}$, which are three closely spaced tones, widening the affected region and increasing the likelihood of disrupting multiple satellites simultaneously. The green trace depicts wide-band FM jamming, a frequency-modulated emission spanning tens of MHz that broadly raises the noise floor, degrading all channels together.

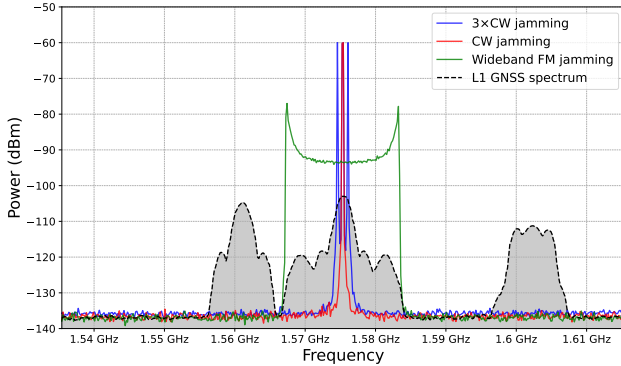


Fig. 1: L1-band jamming profiles overlaid on the GNSS spectrum.

Given L1 band jamming in the form of CW, $3\times\text{CW}$, or wide-band FM, we seek a method with the goal of position error mitigation. Specifically, our goal is to design a model Φ that: (a) operates under any of the three jamming modalities, (b) remains robust across multiple interference power levels, and (c) shows potential for generalization across different receivers.

Considering any given time step t , a typical GNSS receiver observes a variable number N_t of satellites. Each satellite observation provides features such as SNR, azimuth, and elevation, while the receiver also maintains its estimated position $(\text{lat}_t, \text{lon}_t)$. We represent the complete observation set at time t as:

$$O_t = \{(\text{lat}_t, \text{lon}_t), o_{t,1}, \dots, o_{t,N_t}\}, \quad (1)$$

where each $o_{t,i} \in \mathbb{R}^d$ is a d -dimensional feature vector containing the SNR, azimuth, and elevation corresponding to the i -th satellite.

Interference affects these measurements in a time-correlated manner: SNR collapses, tracking is intermittently lost, and the estimated position drifts. Relying on a O_t single time step ignores this temporal structure. Therefore, we seek a model Φ that uses a short history of observations to estimate the receiver's current deviation vector $\hat{Y}_t = (\Delta\text{lat}_t, \Delta\text{lon}_t)$:

$$\hat{Y}_t = \Phi(\{O_{t-k}, \dots, O_t\}) \quad (2)$$

IV. PROPOSED METHOD

A direct approach to the problem defined in Section III is to treat the observation history $\{O_{t-k}, \dots, O_t\}$ as a multivariate

time series. However, this is challenging because the number of visible satellites N_t varies continuously as satellites rise and set, and jamming can cause additional signal dropouts. These factors produce sequences with irregular and dynamic structure, complicating the use of conventional sequence models.

A more intuitive perspective arises from the physical configuration of the system. The receiver–satellite constellation inherently resembles a star-shaped graph network, as the receiver acts as a central node connected to the satellites currently in view.

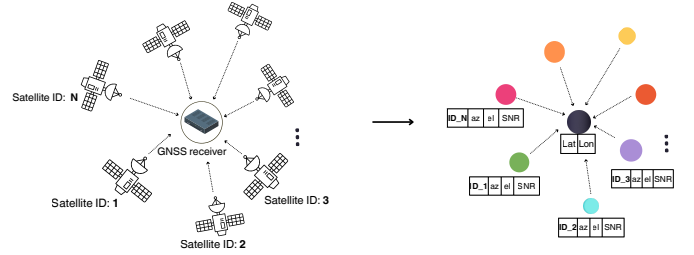


Fig. 2: From physical constellation to graph snapshot

At each time step t , the observation set O_t can be equivalently represented as a heterogeneous star-graph snapshot G_t . Figure 2 illustrates this transformation as the left panel shows the physical GNSS constellation at a given time step, while the right panel depicts the corresponding heterogeneous graph G_t , where V_t contains the receiver and currently visible satellites (with $V_t \neq V_{t+1}$ as satellites rise and set), E_t contains edges from the receiver to tracked satellites, and X_t stores node features, including the receiver's estimated lat_t and lon_t , and each satellite's SNR, azimuth, and elevation.

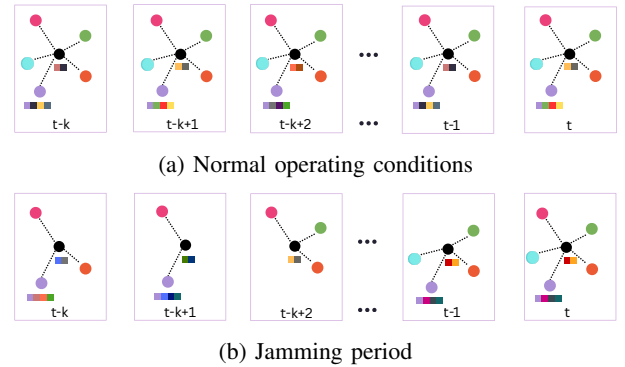


Fig. 3: Temporal graph sequence

To capture evolution over time $\{O_{t-k}, \dots, O_t\}$ from Eq. 2, we adopt the Discrete-Time Dynamic Graphs (DTDG) perspective [24], where a time-varying system is represented as a sequence of static graph snapshots $\{G_{t-k}, \dots, G_t\}$.

Figure 3 illustrates how the constellation evolves over time. Figure 3a shows a sequence of static graph snapshots $\{G_{t-k}, \dots, G_t\}$ under normal operational conditions. In this regime, the overall network topology is relatively stable, and the node attributes, represented by the colored bars next to each node, evolve in a continuous and smooth manner. In contrast, Figure 3b illustrates a sequence of static graph

snapshots $\{G_{t-k}, \dots, G_t\}$ during a jamming period. Here, the topological and feature evolution becomes abrupt and erratic. Satellite tracking status is intermittently lost, causing the edges between the receiver and satellites to disappear suddenly. Simultaneously, the satellite feature vectors, represented as colored bars, become volatile, often showing a rapid collapse in signal measurements like SNR, and the central receiver node's features also become noticeably less stable.

This structured graph representation allows us to frame the mitigation task from Section III as a **temporal dynamic graph regression problem**.

A. Proposed model

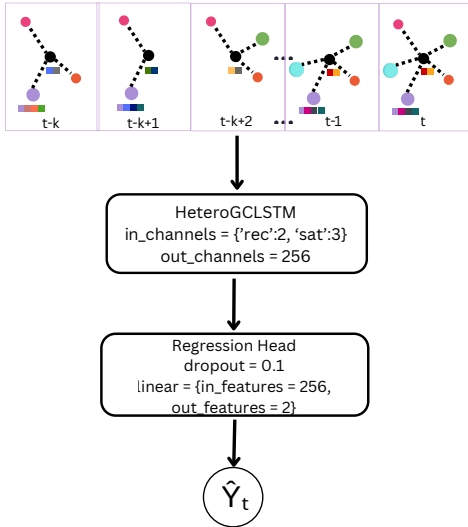


Fig. 4: JaGuard model architecture

To develop the regression function Φ from Eq. 2, we design JaGuard, a spatiotemporal GNN that captures both the geometric structure and temporal evolution of GNSS data under interference. Each input sequence consists of k graph snapshots, each containing one receiver node and a time-varying set of satellite nodes N_t . During jamming, satellites may temporarily disappear or reappear, causing the node set and edge structure to change between consecutive snapshots.

The proposed neural architecture, designed to learn to approximate Φ , employs a single HeteroGCLSTM layer [25]. It explicitly combines graph convolution with recurrent memory gates. Specifically, four HeteroConv sub-layers produce the inputs for the LSTM gates: input, forget, output, and the cell-state candidate. In this way, each node first aggregates spatial context from its one-hop neighborhood before the temporal update. The standard LSTM equations then compute gate activations and update the cell and hidden states (c_τ, h_τ) from $(c_{\tau-1})$ and the current graph features.

The complete model architecture is illustrated in Fig. 4. The figure shows how the sequence of dynamic graph snapshots, each with input features defined by `in_channels = 'rec': 2, 'sat': 3`, is sequentially processed by the HeteroGCLSTM layer. The receiver's final hidden state is then fed into the regression head to yield the predicted horizontal deviation \hat{Y}_t .

We utilized a single HeteroGCLSTM layer, which was a choice justified by the star-graph topology inherent to the problem. The single layer allows a node to aggregate information from its one-hop neighborhood [26], and additional layers would not extend the receiver's receptive field as they would simply reprocess the same one-hop messages at a higher cost.

The overall model works by unrolling the HeteroGCLSTM layer, which maps inputs to a 256-dimensional hidden space, through the input window of k graph snapshots. The final hidden state of the receiver node (h_t), which summarizes the relevant spatiotemporal history, is passed to a regression head. This head consists of a dropout layer ($p = 0.1$) for regularization, followed by a linear layer that maps the 256-dimensional representation to the 2-dimensional output. No activation function is applied to the output layer, since range-restricting nonlinearities would limit the ability to represent the full range of real-valued deviations, thus yielding the predicted deviation \hat{Y}_t from Eq. 2.

V. METHODOLOGY AND EXPERIMENTAL DETAILS

To outline the specifics of our work, first, we explain the process of dataset preparation and then show the details of the model training and evaluation processes.

A. Dataset

To evaluate our method, we utilized the dataset introduced by Blatnik et al. [23], which comprises multivariate time series of GNSS observations collected through a conducted testing framework. Two distinct physical receivers were used for data collection, to ensure hardware diversity in signal reception and response behavior: a U-blox MAX-M10 (10-Series) and an Ai-Thinker GP01. While the U-blox 10 supports GPS, GLONASS, Galileo, BeiDou, and QZSS, and the GP01 supports GPS, BeiDou, and either Galileo or GLONASS, our analysis is restricted exclusively to GPS observations to maintain a consistent baseline across devices. The experimental framework employed synthesized RF interference to establish a controlled testing environment. Interference was introduced with three jamming modalities: Continuous Wave (CW), multi-tone Continuous Wave ($3 \times CW$), and wideband FM, at six power levels from -45 to -70 dBm. For **U-blox 10**, data is available for all three modalities, while for **GP01**, only CW and $3 \times CW$ are available, as the receiver produced no usable output under FM jamming.

To characterize receiver stability, every unique combination of receiver, jammer, and power level was repeated 50 times. Each repetition followed a strict temporal protocol: an initial 100s period with no interference, followed by 100s with the jammer active, and a final 80s recovery phase. Data were sampled at approximately 1 Hz, producing a time-ordered multivariate sequence that reflects evolving satellite visibility and signal quality [23]. While in theory these repetitions of a deterministic process should yield identical results, in practice, the receiver's internal logic and real-time processing introduce slight behavioral variations in each run. This non-deterministic response provides a rich and realistic dataset that reflects the stochastic nature of real-world signal processing. The

inherent unpredictability of the GNSS receiver’s response to a disturbance is illustrated in Figure 5. It presents 50 repeated measurements of the GP01 receiver’s positional deviation in response to a jamming signal, present at times denoted as the shaded red area. Each colored line represents an individual measurement. The first and last 100s show an undisturbed environment, highlighting repeatability and recovery after the disturbance.

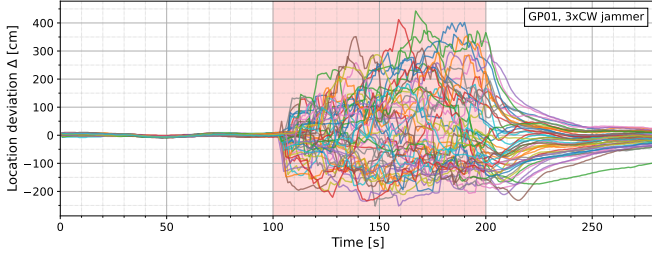


Fig. 5: Positional deviation of the GP01 GNSS receiver across 50 repeated measurements under $3\times\text{CW}$ jamming.

To emulate operational conditions where the type and strength of interference vary unpredictably, we also construct a *mixed* set for each receiver. For each device, sequences are pooled across its available jamming modalities and all power levels, with approximately balanced sampling to avoid over-representing any single condition. Retaining the standard measurement protocol, these heterogeneous sets allow us to assess model robustness under diverse interference and evaluate cross-device generalization by training on one receiver and testing on the other.

To evaluate performance under the most demanding conditions, we prepared a “worst-case” dataset for each receiver. Each dataset consists of 50 measurement sequences recorded at the highest jammer power level of -45 , dBm. The sequences combine all interference types available for that receiver (CW, $3\times\text{CW}$, and FM for U-blox 10; CW and $3\times\text{CW}$ for GP01). These datasets provide a rigorous stress test, designed to examine whether the model can generalize across different threat types and perform reliably during maximum signal disruption.

To convert these raw time-series sequences into inputs for spatio-temporal learning, each timestamp is transformed into a structured graph snapshot as detailed in Section III. This snapshot-based formulation naturally encodes both the heterogeneity of the interaction space, with different node types and distinct feature sets, and its dynamics, including time-varying topology and signal attributes, within the satellite-receiver interaction space.

B. Model training and evaluation

For each experimental scenario described in Section V-A, the 50 measurement repetitions were divided into training and test sets using a standard 80:20 ratio. A portion of the training set was held out as a validation set to monitor performance during training and prevent overfitting. Input sequences were generated using a sliding window approach with both a

window size and stride of 10. These hyperparameters were selected based on a dedicated ablation study.

The model parameters were updated using the Adam optimizer, a standard adaptive learning rate algorithm designed to efficiently find the minimum of the loss function. The optimizer was configured with an initial learning rate of 10^{-3} and a weight decay value of 10^{-2} , which applies L2 regularization to reduce overfitting. These values were determined empirically to achieve stable and effective training.

As a loss function, we utilized Smooth L1 Loss, also known as the Huber Loss. A key advantage of this function is the stability it provides during training, particularly in the presence of outliers. For the sudden, large position deviations characteristic of interfered GNSS signals, the loss grows linearly rather than quadratically. This approach ensures that large errors are still strongly penalized, but it avoids the disproportionately large gradients that can destabilize the learning process. The transition point β between the linear and quadratic behavior was set to 10^{-2} in our experiments, as this value was empirically found to provide the most stable training convergence.

The training process is further regulated with an Early Stopping mechanism that halts training if the validation loss ceases to improve. The model checkpoint with the best performance on the validation set was saved and used for the final evaluation on the held-out test set. To mitigate the effects of random initialization, each model was trained with five different random seeds. The results presented are averages and standard deviation (STD) across the five runs.

For evaluation, we selected metrics that directly quantify the positional prediction error in a physically interpretable manner. We calculate the Mean Absolute Error (MAE) for latitude and longitude, as per:

$$MAE_{lat} = \frac{1}{M} \sum_{i=1}^M |\Delta lat_i - \widehat{\Delta lat}_i| \quad (3)$$

$$MAE_{lon} = \frac{1}{M} \sum_{i=1}^M |\Delta lon_i - \widehat{\Delta lon}_i| \quad (4)$$

where M is the total number of samples in the evaluation set, Δlat_i and Δlon_i are the true deviation values for the i -th sample, and $\widehat{\Delta lat}_i$ and $\widehat{\Delta lon}_i$ are the corresponding deviation values predicted by the model. These metrics measure the average error along each orthogonal axis, providing insight into any directional bias in the predictions.

To provide a unified measure of the 2D positioning error, we calculate the average Euclidean distance between the predicted and true deviation vectors. We refer to this as the Euclidean MAE (MAE_{euc}), defined as:

$$MAE_{euc} = \frac{1}{M} \sum_{i=1}^M \sqrt{(\Delta lat_i - \widehat{\Delta lat}_i)^2 + (\Delta lon_i - \widehat{\Delta lon}_i)^2} \quad (5)$$

where the terms under the square root represent the squared errors in the latitude and longitude dimensions for the i -th sample.

All error metrics are reported in centimeters (cm), providing a clear and direct assessment of the model’s effectiveness in mitigating position deviations.

C. Comparison to the baseline models

To evaluate our proposed JaGuard architecture, we compare its performance with three baseline models that operate directly on the multivariate time series representation (SNR, Azimuth, Elevation, Longitude, and Latitude) of the GNSS data. To ensure a fair comparison, both the raw time series for the baseline models and the corresponding graph sequences for our proposed model were segmented using a sliding window of size 10, with a stride equal to the window size to create non-overlapping samples. Any missing values within the time-series windows were handled by zero-padding, corresponding to situations in which a previously tracked satellite becomes temporarily non-visible and therefore provides no valid measurements.

Our first baseline is TSMixer [27], a fully-connected linear model. This architecture serves as a strong baseline for time series regression tasks, as established by recent research [27]. We retain its standard architecture, in which the input window is first flattened into a vector, and the model output is adjusted to predict our 2-unit target.

Our second baseline is a modern, uniform CNN model, another strong alternative for time series regression tasks, evaluated in the same research as the previous model [27]. This architecture is composed of a stack of four identical blocks, designed to process the input time series sequentially. We adopt this model to provide a direct comparison with the MLP-style TSMixer, testing the benefits of local feature extraction through convolution. The architecture remains consistent with the original model, where the output from the final block is flattened and passed to an output layer to predict our 2-unit target.

To directly examine whether more advanced deep learning architectures designed for regression tasks provide an advantage on this problem, our third baseline is a deep, hierarchical CNN. This custom architecture is inspired by the sequence-to-point (Seq2Point) model [28]. In contrast to the uniform CNN, this model uses a heterogeneous stack of five consecutive Conv1D layers with decreasing kernel sizes. The motivation is to determine whether a more hierarchical feature extraction approach offers a performance advantage over the simpler, uniform CNN for our specific GNSS dataset. The output is similarly flattened and passed through a final Dense layer to the 2-unit output layer.

D. Comparative Analysis of Training Sample Ratios

To further highlight the advantages of our proposed model over the baselines, especially in terms of performance and data efficiency, we conducted an additional experiment in which we analyze the effects of different test-train split ratios. The experiment was conducted utilizing random shuffle splits across a range of ratios from 10:90 to 90:10 with a step of 10. At each split, the experiments were repeated ten times.

E. Ablation study

To systematically evaluate the impact of key hyperparameters and justify our architectural choices presented in Section IV-A, we conducted a comprehensive ablation study. The primary goals of this study were to determine the optimal input window size for capturing temporal dynamics and to assess the effect of the model’s hidden layer dimensionality on its predictive performance. The study was carried out on the most challenging interference scenarios common to both receiver types: the Continuous Wave (CW) and multi-tone Continuous Wave ($3\times$ CW) jamming modes at their highest power level of -45 dBm.

We evaluated a range of window sizes: 5, 10, 14, 20, 28, 35, 40, 56, 70, and 140. These values were specifically chosen as they are divisors of the total 280s measurement duration. To prevent data redundancy and ensure that each data point contributes uniquely to the training process within an epoch, we employed non-overlapping windows by setting the stride equal to the window size in each experiment.

Our model architecture employs a single graph convolutional recurrent layer (HeteroGCLSTM), since in the star-shaped receiver-satellite topology one hop already connects the receivers to all visible satellites, as explained in Section IV-A. Therefore, instead of varying the model’s depth, we focused on the impact of its hidden size. We experimented with different sizes for the hidden dimension, training and evaluating separate models with dimensions of 16, 32, 64, 128, and 256 to examine the impact of model complexity on performance.

VI. RESULTS

In this section, we evaluate the performance of our proposed approach. The details of the experimental setup used to obtain the results are described in Section V.

A. Overall performance analysis

This section presents the performance evaluation of the proposed JaGuard model, in comparison with three established baseline models: Seq2Point, TSMixer, and a conventional, uniform CNN. The analysis is conducted at a fine-grained level, providing a detailed breakdown of results by jamming type and power level for each receiver.

Tables II and III present the per-receiver results. Rows are organized by jamming type (U-blox 10: CW, $3\times$ CW, FM; GP01: CW, $3\times$ CW), with each method shown as a sub-row. Columns list jammer power levels, sweeping from -45 to -70 dBm. For each jamming block, the final two rows report the unmitigated pre-correction error and the corresponding percentage error reduction achieved by the proposed model at that power level.

For the U-blox 10 receiver, Table II shows that our proposed JaGuard consistently outperforms all baselines across CW, $3\times$ CW, and FM jamming throughout the entire power sweep. In the high-interference regime (-45 dBm), it achieves the lowest errors: 4.41 ± 0.49 cm (CW), 4.84 ± 0.48 cm ($3\times$ CW), and 4.82 ± 0.51 cm (FM). The baselines show larger initial errors; Seq2Point yields 6.60 ± 1.21 cm (CW), 5.52 ± 0.44 cm ($3\times$ CW), and 7.13 ± 0.53 cm (FM). TSMixer

Jamming	Method	-45 dBm	-50 dBm	-55 dBm	-60 dBm	-65 dBm	-70 dBm
CW	JaGuard (proposed)	4.41 ± 0.49	3.52 ± 0.28	2.28 ± 0.39	1.96 ± 0.19	1.81 ± 0.19	1.65 ± 0.21
	Seq2Point	6.60 ± 1.21	4.82 ± 0.27	3.52 ± 0.46	3.01 ± 0.17	2.55 ± 0.32	2.23 ± 0.21
	TSMixer	7.17 ± 0.64	5.72 ± 0.54	4.20 ± 0.67	3.49 ± 0.28	2.81 ± 0.34	2.53 ± 0.19
	CNN	8.82 ± 1.06	6.77 ± 0.92	4.49 ± 0.62	3.99 ± 0.56	3.64 ± 0.62	2.72 ± 0.29
	Unmitigated Error (cm)	102.07	81.61	53.87	47.26	44.67	41.36
	Error Reduction (proposed) (%)	95.68	95.69	94.65	95.85	95.95	96.01
3×CW	JaGuard (proposed)	4.84 ± 0.48	4.09 ± 0.35	3.49 ± 0.68	2.96 ± 0.59	2.87 ± 0.53	3.35 ± 0.27
	Seq2Point	5.52 ± 0.44	5.48 ± 0.28	4.47 ± 0.59	3.54 ± 0.53	3.29 ± 0.59	4.83 ± 0.42
	TSMixer	6.38 ± 0.24	5.97 ± 0.28	5.01 ± 0.29	3.87 ± 0.47	3.71 ± 0.34	6.59 ± 0.38
	CNN	5.99 ± 0.43	6.12 ± 0.97	5.87 ± 1.17	3.71 ± 0.21	4.15 ± 1.66	6.08 ± 0.92
	Unmitigated Error (cm)	116.24	107.48	102.82	94.79	95.05	83.77
	Error Reduction (proposed) (%)	95.84	96.19	96.61	96.88	96.98	96.00
FM	JaGuard (proposed)	4.82 ± 0.51	3.72 ± 0.48	2.80 ± 0.39	2.49 ± 0.53	2.29 ± 0.21	1.90 ± 0.10
	Seq2Point	7.13 ± 0.53	5.79 ± 0.61	4.79 ± 0.51	5.24 ± 0.34	3.44 ± 0.24	3.04 ± 0.34
	TSMixer	9.48 ± 0.87	7.37 ± 0.39	5.97 ± 0.57	6.09 ± 0.33	4.16 ± 0.34	3.60 ± 0.48
	CNN	12.33 ± 1.44	8.98 ± 1.17	6.38 ± 1.03	5.68 ± 0.78	4.68 ± 0.58	4.14 ± 1.04
	Unmitigated Error (cm)	120.50	114.65	98.23	89.21	64.11	44.05
	Error Reduction (proposed) (%)	96.00	96.76	96.71	96.30	95.82	95.69

TABLE II: U-blox 10 — Average Euclidean MAE (cm) ± SD across 5 seeds by jamming type and power.

Jamming	Method	-45 dBm	-50 dBm	-55 dBm	-60 dBm	-65 dBm	-70 dBm
CW	JaGuard (proposed)	3.64 ± 0.97	3.53 ± 1.43	1.76 ± 0.11	1.64 ± 0.26	1.55 ± 0.34	1.59 ± 0.43
	Seq2Point	5.03 ± 0.32	7.63 ± 1.97	2.35 ± 0.27	2.57 ± 0.47	1.96 ± 0.36	2.63 ± 1.81
	TSMixer	5.70 ± 0.30	6.97 ± 1.26	2.62 ± 0.13	2.96 ± 0.57	1.81 ± 0.22	2.24 ± 0.92
	CNN	6.47 ± 0.98	9.66 ± 2.64	2.75 ± 0.44	2.83 ± 0.25	2.63 ± 0.64	4.63 ± 4.52
	Unmitigated Error (cm)	277.51	298.82	289.29	280.82	277.70	264.45
	Error Reduction (proposed) (%)	98.69	98.29	98.56	99.35	99.40	99.33
3×CW	JaGuard (proposed)	7.74 ± 0.69	2.50 ± 0.15	2.81 ± 0.55	1.83 ± 0.28	2.21 ± 0.32	1.76 ± 0.15
	Seq2Point	10.45 ± 0.53	4.51 ± 0.39	4.85 ± 0.57	2.57 ± 0.19	3.27 ± 0.33	3.37 ± 1.26
	TSMixer	11.40 ± 0.72	4.99 ± 0.15	5.17 ± 0.43	2.87 ± 0.18	3.44 ± 0.22	2.92 ± 0.60
	CNN	11.29 ± 0.87	5.18 ± 0.73	6.57 ± 0.42	3.54 ± 0.76	4.39 ± 1.04	4.32 ± 1.70
	Unmitigated Error (cm)	255.07	293.18	293.99	282.22	286.14	276.98
	Error Reduction (proposed) (%)	96.97	97.92	98.96	99.31	99.19	99.25

TABLE III: GP01 — Average Euclidean MAE (cm) ± SD across 5 seeds by jamming type and power.

follows with 7.17 ± 0.84 cm (CW), 6.12 ± 0.37 cm (3×CW), and 7.98 ± 0.54 cm (FM), while the CNN exhibits the largest errors across most settings (e.g., 12.33 ± 1.44 cm on FM at -45 dBm). As interference weakens, errors generally decrease into the 2–3 cm range, with JaGuard reaching its lowest error floor at -70 dBm: 1.65 ± 0.21 cm (CW) and 1.90 ± 0.10 cm (FM). The Error Reduction rows confirm that JaGuard delivers over 95% reduction relative to the unmitigated case across all powers and jamming types.

For the GP01 receiver, Table III proves that the performance trends are consistent, confirming the robustness of the proposed architecture. At the highest interference level (-45 dBm), JaGuard achieves the lowest errors: 3.64 ± 0.97 cm (CW) and 7.74 ± 0.69 cm (3×CW), confirming that the multi-tone case is inherently more challenging. The baselines exhibit higher errors: Seq2Point achieves 5.03 ± 0.32 cm (CW) and 8.44 ± 0.41 cm (3×CW); TSMixer follows with 5.39 ± 0.49 cm (CW) and 9.36 ± 0.44 cm (3×CW). The

CNN generally performs the worst, showing the largest errors and standard deviations (e.g., 3×CW: 11.29 ± 0.87 cm), indicating less stable training under high interference. Performance improves nearly monotonically as power decreases, with JaGuard reaching its error floor at -70 dBm: 1.59 ± 0.43 cm (CW) and 1.76 ± 0.15 cm (3×CW).

In summary, JaGuard achieves the best performance across both receivers, jamming types, and power levels, with the lowest errors, especially in high-interference regimes. The ranking of models is consistent: JaGuard outperforms Seq2Point, which in turn outperforms TSMixer, while the standard CNN performs worse. This order reflects their architectural capabilities: JaGuard utilizes dynamic graph structures to capture relationships that time-series models like Seq2Point and TSMixer are unable to, whereas the CNN lacks sufficient temporal abstraction. Among interference types, 3×CW is more challenging than CW due to its wider spectral impact. FM resembles CW at low power but becomes harsher at

high power as it broadly raises the noise floor. Variability across seeds is small for the top three models, with occasional instability observed only in the CNN.

B. Mixed dataset

To mimic operational conditions where interference type and strength vary, we prepared a mixed dataset per receiver by pooling all available jamming types across power levels (-45 to -70 dBm). Table IV reports mean Euclidean MAE (cm) \pm STD over five seeds. As it can be seen in Table IV, JaGuard achieves the lowest error on both receivers: 4.25 ± 0.31 cm on U-blox 10 and 3.78 ± 0.27 cm on GP01, improving over the next-best baseline Seq2Point, which achieves 5.12 ± 0.44 cm on U-blox 10 and 4.50 ± 0.19 cm on GP01, which is approximately 21% and 19% worse than our baseline, respectively. TSMixer follows with 5.82 ± 0.53 cm on U-blox 10 and 5.05 ± 0.87 cm on GP01, while CNN has the largest errors at 6.78 ± 0.82 cm and 8.26 ± 1.08 cm. Standard deviations are small across all models, indicating stable behavior over seeds.

Model	U-blox 10 (cm)	GP01 (cm)
Proposed - JaGuard	4.25 ± 0.31	3.78 ± 0.27
Baseline — TSMixer	5.82 ± 0.53	5.05 ± 0.87
Baseline — Seq2Point	5.12 ± 0.44	4.50 ± 0.19
Baseline — CNN	6.78 ± 0.82	8.26 ± 1.08

TABLE IV: Mixed dataset—all jamming types pooled across powers -45 to -70 dBm.

To evaluate the transferability of our models between different GNSS receivers, we conduct a cross-device generalization test by training the proposed model on one receiver’s data and testing it on the other’s. Table V reports the Euclidean MAE results of this experiment. When trained on U-blox 10, the model achieves a strong MAE of 4.25 cm on the source dataset and transfers well to GP01 with a MAE value of 2.89 cm. When trained on GP01, it attains 3.78 cm on the source dataset but degrades on U-blox 10 (8.21 cm). This asymmetry arises from a jammer-type shift, as the GP01 dataset contains only CW and $3 \times$ CW jamming types, whereas the U-blox 10 dataset also includes wideband FM. Consequently, the GP01-trained model encounters previously unseen FM jamming on U-blox 10, while the U-blox 10-trained model has seen all three types and transfers more effectively. However, for the GP01 to U-blox 10 transfer, the achieved error of ≈ 8 cm is acceptable for our mitigation setting and indicates that the model retains useful predictive power even under unseen interference.

Trained on	Evaluated on	Euclidean MAE (cm)
U-blox-10	GP01	2.89
GP01	U-blox 10	8.21

TABLE V: Cross-device generalization of JaGuard.

C. Analysis of Training Sample Ratios on Model Performance

To quantify sensitivity to training data volume, we ran each baseline and our proposed model ten times with different

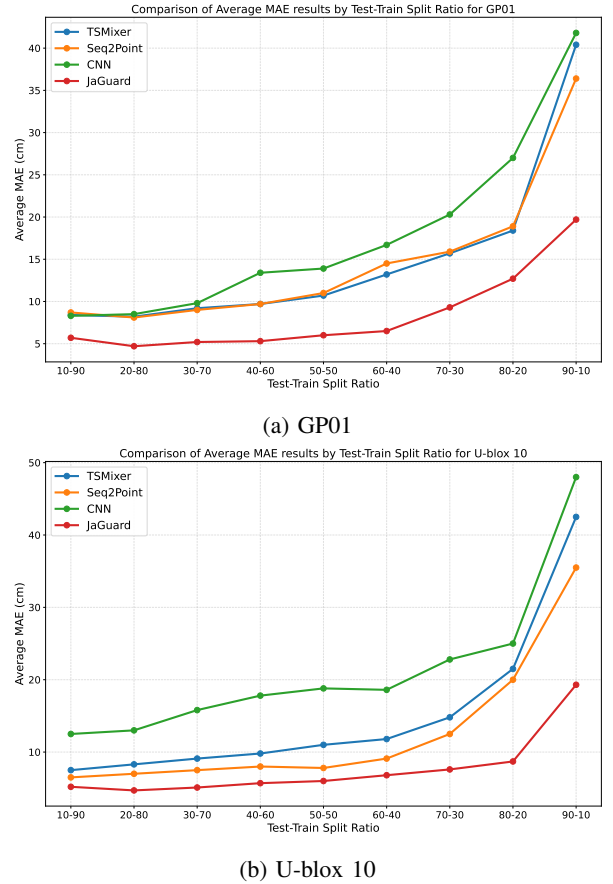


Fig. 6: Comparison of Average MAE by test-train split.

test–train split ratios, ranging from 90:10 to 10:90 in steps of 10, and report the average MAE across runs for both GP01 and U-blox 10. This analysis was conducted on the “worst-case” scenario datasets described in Section V-A, which combine all available interference types at the maximum jammer power level of -45 dBm, ensuring a rigorous stress test of model generalization.

Figure 6 illustrates how the ratio of testing to training data affects model performance. The plots report average MAE per receiver. Figure 6a shows the MAE curves of the proposed and baseline models for the GP01 receiver. As expected, the MAE values for all four models gradually increase as the proportion of training data decreases. This figure also shows us one of the main advantages of our proposed architecture. Even when using only 10% of the available data for training, it achieves a MAE of around 20 cm, while the baseline models in this case achieve scores in the range of 36–42 cm. This trend continues for other ratios, demonstrating that our approach requires considerably less training data to achieve higher model performance compared to the baselines, due to the graph-based perspective of this problem.

For U-blox 10, we observe in Figure 6b that the trend remains similar. As the split shifts from 90:10 to 10:90, all curves drop, and the proposed model remains ahead across most splits. At the 10:90 split, our proposed and the strongest

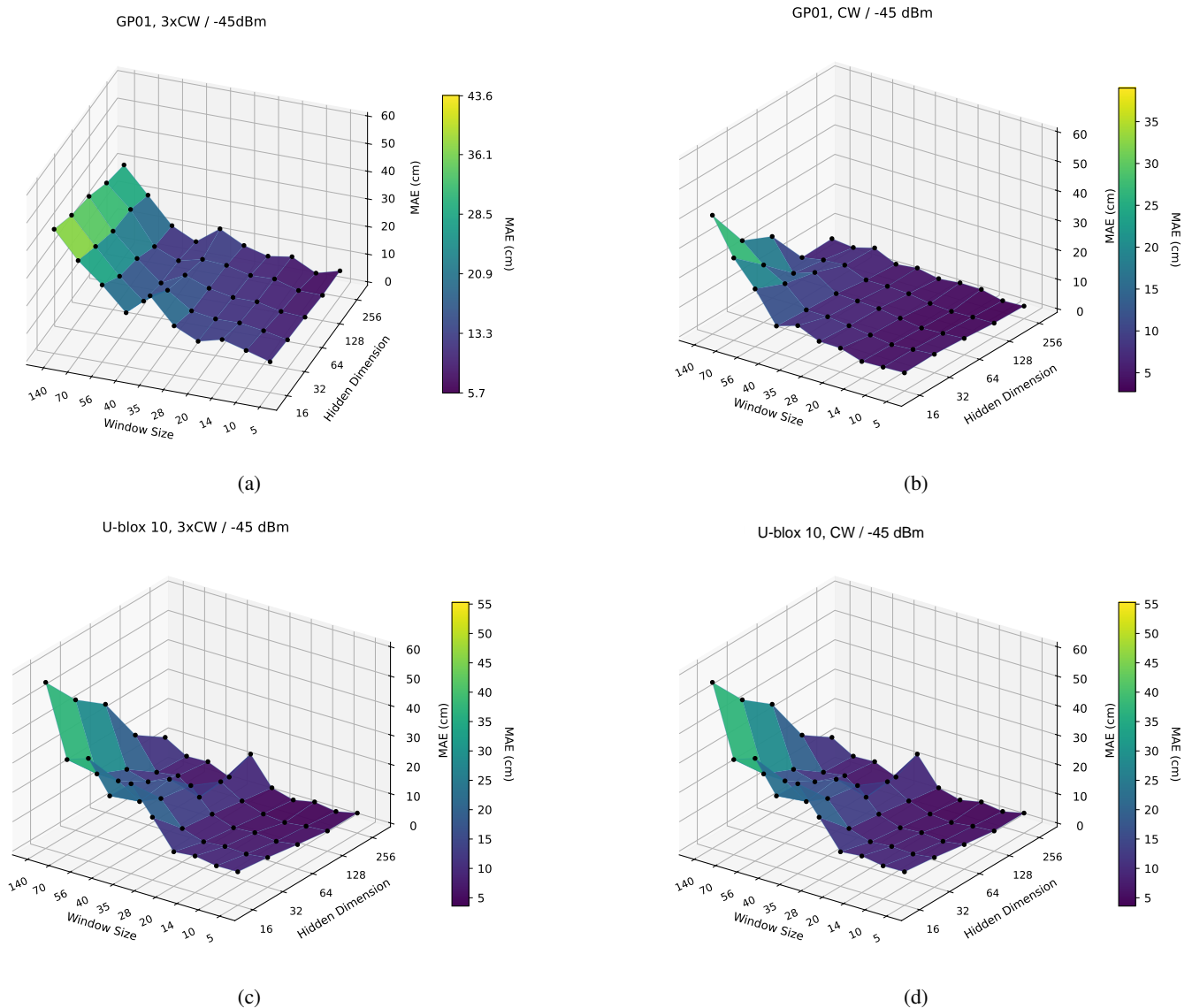


Fig. 7: 3D surfaces of MAE (cm) as a function of input window size and hidden dimension for both receivers (GP01, U-blox 10) under CW and $3\times$ CW jamming at -45 dBm (darker the better).

Seq2Point baseline model achieve very similar MAE scores. Despite this narrow gap in the high training data range, the proposed model still maintains a clear lead in the low training data range.

D. Ablation study

Figure 7 illustrates the 3D response surfaces of MAE (cm) for two receivers under the most challenging interference regimes, CW and $3\times$ CW at -45 dBm, as a function of input window sizes and hidden dimensions. In Figure 7a (GP01 under CW), MAE decreases for short windows of past constellation snapshots, then worsens as the input history grows. Larger hidden layers help up to about 128–256 units, with diminishing returns beyond 128. Nonetheless, we adopt 256 because the incremental accuracy is operationally meaningful for our mitigation task, while hidden dimension sizes beyond 256 result in unfavorable computational complexity. The op-

timum occurs at a window of 10 s and a hidden dimension of 256, yielding MAE = 2.74 cm. Figure 7b (GP01 under $3\times$ CW) follows the same pattern but at a higher error level, as multi-tone interference is more challenging. Here, the best setting is again a window of 10 s and a hidden dimension of 256, with MAE = 7.39 cm.

In Figure 7c (U-blox 10 under CW), the surface shows a broader range and a steeper penalty for long windows than GP01, yet the low-error area remains at short windows and larger hidden sizes. The minimum is at a window size of 10 s, and a hidden dimension 256, MAE = 3.97 cm. Finally, Figure 7d (U-blox 10 under $3\times$ CW) mirrors these trends, with the optimum again at a window of 10 s, and a hidden dimension of 256, MAE = 4.59 cm.

These observations reveal several trends. The crucial factor across all tests is the input window size, where the error consistently decreases for short windows and deteriorates

as the window grows. The best regions are around 10–20 s windows, after which MAE rises for windows of 28–140 s. Increasing the hidden dimension yields clear gains from 16/32 to 64/128, and smaller but still visible improvements up to 256. In other words, adding capacity is beneficial, but the marginal utility flattens beyond 128 units. Surfaces for $3 \times CW$ sit above those for CW, reflecting the increased difficulty of multi-tone interference, which is consistent with the results in Section VI-A.

Compared to GP01, U-blox 10 spans a broader MAE range, reaching the top of the color scale, paying a sharper price for longer windows, while GP01, especially under CW, remains comparatively flat. Overall, the most dependable low-error regime clusters around window lengths of 10–20 s and hidden dimensions of 128–256. Accordingly, the ablation results support our selection of a 10 s window and a 256-dimensional hidden layer size, as specified in Section IV-A.

VII. OPERATIONAL BOUNDARIES AND LIMITATIONS

A key design choice in GNSS jamming mitigation is where to apply corrections. Some systems correct raw measurements to preserve internal integrity checks, but we instead operate in the position domain to address the constellation-wide degradation caused by jamming. Traditional integrity logic is built to detect and exclude isolated faults, however as jamming reduces the quality of all satellites simultaneously, so standard exclusion would often discard every measurement and terminate navigation.

By correcting the final position, our JaGuard model captures the aggregate distortion while keeping the receiver producing a solution. This design decouples the correction from internal integrity checks and requires the receiver to output a valid, though biased, longitude and latitude. In cases of complete tracking loss, such as strong jamming beyond about -40 dBm, no longitude and latitude is available and the JaGuard method cannot operate, which is an inherent limitation. Overall, the approach enhances resilience in degraded conditions rather than replacing integrity mechanisms.

VIII. CONCLUSIONS

In this work, we presented a receiver-centric formulation of GNSS jamming mitigation as a dynamic graph regression problem, and introduced JaGuard, a deep temporal graph network that estimates horizontal position deviation.

Across two receivers, multiple jamming modalities and power levels, JaGuard consistently outperforms strong time-series baselines: TSMixer, CNN and Seq2Point. The advantage holds both in per-scenario evaluations and on mixed datasets that combine all power levels and jamming types per receiver. The advantage is most pronounced under strong interference (e.g., U-blox 10/FM at -45 dBm), where JaGuard demonstrates greater resilience to high-power signal disruption and maintains minimal variance between training seeds.

Sensitivity analyses with varying test-train ratios further indicate good data efficiency as the proposed model remains competitive when training data are scarce and maintains the leading envelope as more data become available.

Cross-device tests also show that both directions are viable. While training on U-blox 10 yields the strongest transfer to GP01 (2.89 cm), the reverse direction remains competitive. A model trained only on GP01 still attains ≈ 8.2 cm on U-blox 10, despite never seeing FM jamming during training. These results argue for broad coverage across devices and jamming types, but also show that useful generalization is achievable under coverage mismatch.

Overall, the results indicate that dynamic graph modeling is a novel and strong paradigm for GNSS interference mitigation, offering accurate, stable error estimates that can be used for real-time correction, quality flagging, or adaptive weighting within positioning pipelines.

ACKNOWLEDGEMENTS

This work was supported by the Slovenian Research Agency (P2-0016).

REFERENCES

- [1] J. Li, K. K. Nagalapur, E. Stare, S. Dwivedi, S. A. Ashraf, P.-E. Eriksson, U. Engström, W.-H. Lee, and T. Lohmar, "5g new radio for public safety mission critical communications," *IEEE Communications Standards Magazine*, vol. 6, no. 4, pp. 48–55, 2023.
- [2] G. Workgroup, "Gps spoofing: Final report of the gps spoofing workgroup," *GPS Spoofing WorkGroup: London, UK*, 2024.
- [3] H. Biswas, "Cyber security in power grid networks, at the crossover domain intersection," in *2024 IEEE 5th India Council International Subsections Conference (INDISCON)*. IEEE, 2024, pp. 1–6.
- [4] A. Brighente, M. Conti, M. Schotsman, and S. Sciancalepore, "Obfuscated location disclosure for remote id enabled drones," *IEEE Transactions on Dependable and Secure Computing*, pp. 1–18, 2025.
- [5] L. Xiong, R. Kang, J. Zhao, P. Zhang, M. Xu, R. Ju, C. Ye, and T. Feng, "G-vido: A vehicle dynamics and intermittent gnss-aided visual-inertial state estimator for autonomous driving," *IEEE Transactions on Intelligent Transportation Systems*, vol. 23, no. 8, pp. 11 845–11 861, 2021.
- [6] E. Bermudez, L. Lins, P. Pereira, and P. Maciel, "A stochastic model for evaluating the aging impact on satellite systems' availability," *IEEE Transactions on Dependable and Secure Computing*, vol. 22, no. 5, pp. 4942–4953, 2025.
- [7] T. Morong, P. Puričar, and P. Kovář, "Study of the gnss jamming in real environment," *International Journal of Electronics and Telecommunication*, vol. 65, no. 1, pp. 65–70, 2019.
- [8] M. García-Bermúdez, J. Solé-Lloveras, and M. A. Azpúrua, "Characterization of illegally marketed gnss jammers," in *2025 ESA Workshop on Aerospace EMC (Aerospace EMC)*. IEEE, 2025, pp. 1–6.
- [9] N. Gerrard, A. Rødningsby, A. Morrison, N. Sokolova, and C. Rost, "Exploration of unintentional gnss rfi sources: Causes, occurrence rates, and predicted future impact," in *Proceedings of the 35th International Technical Meeting of the Satellite Division of The Institute of Navigation (ION GNSS+ 2022)*, 2022, pp. 3925–3934.
- [10] D. Borio and C. Gioia, "Interference mitigation: impact on gnss timing," *GPS Solutions*, vol. 25, no. 2, p. 37, 2021.
- [11] H. Li, Y. Xie, X. Meng, S. Wu, J. Xu, and X. Wang, "A novel method for anomaly detection and correction of gnss time series," *Measurement Science and Technology*, vol. 36, no. 1, p. 016330, 2024.
- [12] Q. Liu, C. Gao, R. Shang, Z. Peng, R. Zhang, L. Gan, and W. Gao, "Nlos signal detection and correction for smartphone using convolutional neural network and variational mode decomposition in urban environment," *GPS Solutions*, vol. 27, no. 1, p. 31, 2023.
- [13] Y. Zhou, X. He, S. Wang, S. Hu, X. Sun, and J. Huang, "Hybrid gnss time-series prediction method based on ensemble empirical mode decomposition with long short-term memory," *Discover Applied Sciences*, vol. 7, no. 1, p. 61, 2025.
- [14] A. V. Kanhere, S. Gupta, A. Shetty, and G. Gao, "Improving gnss positioning using neural-network-based corrections," *NAVIGATION: Journal of the Institute of Navigation*, vol. 69, no. 4, 2022.
- [15] Y. Xia, S. Pan, X. Meng, W. Gao, F. Ye, Q. Zhao, and X. Zhao, "Anomaly detection for urban vehicle gnss observation with a hybrid machine learning system," *Remote sensing*, vol. 12, no. 6, p. 971, 2020.

- [16] I. E. Mehr and F. Dovis, "A deep neural network approach for classification of gnss interference and jammer," *IEEE Transactions on Aerospace and Electronic Systems*, 2024.
- [17] V. Ivanov, R. C. Wilson, and M. Scaramuzza, "Towards simple machine learning baselines for gnss rfi detection," *arXiv preprint arXiv:2504.07993*, 2025.
- [18] H. Chen *et al.*, "An improved vmd-lstm model for time-varying gnss time series prediction with temporally correlated noise [j]. remote sens. 15 (14)," 2023.
- [19] W. Gao, Z. Li, Q. Chen, W. Jiang, and Y. Feng, "Modelling and prediction of gnss time series using gbd, lstm and svm machine learning approaches." *Journal of Geodesy*, vol. 96, no. 10, 2022.
- [20] C. Zhu, X. Xu, Y. Na, C. Ji, D. Wu, and K. Wei, "Enhancing gnss positioning using transformer-based correction network," in *Proceedings of the 37th International Technical Meeting of the Satellite Division of The Institute of Navigation (ION GNSS+ 2024)*, 2024, pp. 1300–1310.
- [21] A. Mohanty and G. Gao, "Learning gnss positioning corrections for smartphones using graph convolution neural networks," *NAVIGATION: Journal of the Institute of Navigation*, vol. 70, no. 4, 2023.
- [22] Y. Lv, Z. Meng, G. Wang, M. Liu, and E. Yan, "Review of research on satellite clock bias prediction models in gnss," *Remote Sensing*, 2025.
- [23] A. Blatnik and B. Batagelj, "Evaluating gnss receiver resilience: A study on simulation environment repeatability," *Electronics*, vol. 14, no. 9, p. 1797, 2025.
- [24] S. M. Kazemi, R. Goel, K. Jain, I. Kobzyev, A. Sethi, P. Forsyth, and P. Poupart, "Representation learning for dynamic graphs: A survey," *Journal of Machine Learning Research*, vol. 21, no. 70, pp. 1–73, 2020.
- [25] B. Rozemberczki, P. Scherer, Y. He, G. Panagopoulos, A. Riedel, M. Astefanoaei, O. Kiss, F. Beres, G. Lopez, N. Collignon *et al.*, "Pytorch geometric temporal: Spatiotemporal signal processing with neural machine learning models," in *Proceedings of the 30th ACM international conference on information & knowledge management*, 2021, pp. 4564–4573.
- [26] H. Gao, F. Yang, Y. Yang, Y. Xu, and Y. Su, "Adaptive receptive field graph neural networks," *Neural Networks*, p. 107658, 2025.
- [27] S.-A. Chen, C.-L. Li, N. Yoder, S. O. Arik, and T. Pfister, "Tsmixer: An all-mlp architecture for time series forecasting," *arXiv preprint arXiv:2303.06053*, 2023.
- [28] C. Zhang, M. Zhong, Z. Wang, N. Goddard, and C. Sutton, "Sequence-to-point learning with neural networks for non-intrusive load monitoring," in *Proceedings of the AAAI conference on artificial intelligence*, vol. 32, no. 1, 2018.